# Comparison of EHD-Driven Instability of Thick and Thin Liquid Films by a Transverse Electric Field

**Payam Sharifi**[1]**, Asghar Esmaeeli**[2]

**Abstract:**   This study aims to explore the effect of liquid film thickness on the electrohydrodynamic-driven instability of the interface separating two horizontal immiscible liquid layers. The fluids are confined between two electrodes and the light and less conducting liquid is overlaid on the heavy and more conducting one. Direct Numerical Simulations (DNSs) are performed using a front tracking/finite difference scheme in conjunction with Taylor-Melcher leaky dielectric model. For the range of physical parameters used here, it is shown that for a moderately thick lower liquid layer, the interface instability leads to formation of several liquid columns and as a result of competition between these columns eventually a big column is formed. On the other hand, for a thin lower layer the lower electrode strongly influences the growth of the instability, leading to a short and a longer column that are connected together by a thin liquid film. When the film becomes too thick, more columns are formed, but the fluid system does not reach a steady state because the liquid columns grow so rapidly that they hit the top electrode. The flow structure is examined and the variation of the steady state kinetic energy of the system with the film thickness and the applied electric voltage is explored.

## 1   Introduction

Electrohydrodynamic-driven instability of the interface separating two immiscible fluids finds relevance in a host of industrial processes. Examples include enhancement of heat and mass transfer rates in pool boiling [Zaghdoudi and Lallemand (2002)], production of fine liquid drops from a liquid jet in electrospraying by application of an electric field in the direction of the jet axis [Collins et al. (2008)], and creation of highly precise structures using polymer melts on submicron scales by electrolithography [Chou and Zhuang (1999); Schaffer et al. (2000)]. Early

---

[1] Department of Mechanical Engineering and Energy Processes Southern Illinois University Carbondale, Illinois 62901. Email: psharifi@siu.edu

[2] Department of Mechanical Engineering and Energy Processes Southern Illinois University Carbondale, Illinois 62901. Email: esmaeeli@engr.siu.edu

interest on the interaction of the electric field and liquids stemmed from the naturally occurring phenomena such as deformation and break up of rain drops during thunderstorm [Macky (1931)] and the electric break down of the liquids in optical studies due to air bubbles trapped in the liquid [O'Konski and Thacher (1953); O'Konski and Harris (1957)]. More recent interest is directed toward microfluidic and biofluidic applications [Stone et al. (2004); Zeng and Korsmeyer (2004)]. The electric field is an attractive means in these applications because of its scalability and action from the distance, in addition to the fact that it acts at the surface and, therefore, becomes increasingly dominant at microscale.

In the absence of free volume electric charge, the electric field affects the interface of the two fluids through interfacial electrical stresses that develop due to mismatch of the electric conductivity $\sigma$ and permittivity $\varepsilon$ of the two fluids. The theoretical model that describes the phenomenon fairly well is the so-called Taylor-Melcher "leaky-dielectric model (LDM)", developed concurrently by Taylor and Melcher in the contexts of electrohydrodynamics of drops [Taylor (1966)] and electrohydrodynamic-driven instability of superimposed fluids [Smith and Melcher (1967); Melcher and Schwarz (1968); and Melcher and Smith (1969)]. The theoretical foundation and the mathematical formulation of the model have been well described in the review articles by Melcher and Taylor (1969), Arp et al. (1980), and Saville (1997). The essence of the model is to assume fluids have finite electric conductivities and that the time scale of charge relaxation due to conduction from the bulk to the surface to be much shorter than any process time of interest. The first assumption allows for accumulation of free charges at the interface and, therefore, the possibility of a net interfacial electrical shear force. The second assumption leads to a substantial simplification in the mathematical formulation as the electric field equations will be decoupled from the momentum equation and reduce to quasi-steady state laws. The leaky dielectric model is also referred to as electrohydrodynamic (EHD) theory since it accounts for the hydrodynamic effect that originates from the imbalance of electric shear stresses at the interface.

The theoretical basis of the electric field-driven instability of the interface was laid out in the pioneering study of Melcher (1963) who used the classical linear stability analysis in conjunction with the "electrohydrostatic" (EHS) model. In the framework of this model, the two superimposed fluids are treated either as two perfectly dielectric fluids or a perfectly dielectric fluid and a perfectly conducting one. In either case, there would be no fluid flow at steady state when the interface settles to an equilibrium shape since the EHS theory precludes the imbalance of tangential electric stresses at the interface. Accordingly, the viscosities of the fluids will only play a role in the transient process and do not come to the picture at steady state. The EHS model combined with inviscid flow assumption can lead to significant

simplification of the mathematical formulation. Melcher (1963) used this approach and formulated a closed form solution to determine the criteria for instability of two horizontal superimposed fluids due to a transverse or parallel (with respect to the interface) uniform DC electric field. His analysis shows that the transverse electric field is always destabilizing when the electric field strength is above a critical magnitude.

While EHS model provides insight into the electric-driven interface instability and is useful in predicting the behavior of the interface for some fluid systems, it does not lead to experimentally-backed results in general. This is because the model precludes formation of free charges at the interface, therefore, overlooking the impact of the interfacial electric shear stresses on the dynamics. These stresses tend to create fluid flow even when the interface is stationary [Esmaeeli and Reddy (2011)] and generally tend to stabilize the instability [Yeoh et al. (2007)]. As pointed out by Taylor (1966), the fluids should not be treated as perfect dielectric; rather they should be considered having slight conductivity to allow for accumulation of free electric charge at the interface. The action of the electric field on this charge results in the net electric shear stress, which is overlooked in EHS model. Taylor's theory was coined Taylor-Melcher leaky dielectric model by Saville (1997). For leaky dielectric fluids, the formulation of the problem becomes more involved. Here, the electric conductivities and viscosities of the fluids also come to the picture. The formulation of the electric-driven instability due to a transverse electric field in the framework of the leaky dielectric theory (EHD) was first done by Smith and Melcher (1967). These authors solved the linearized governing equations using the method of normal modes and derived a dispersion relation that should be generally solved numerically to find the growth rate. Similar to the EHS model, the EHD model suggests that the electric field can be destabilizing once it is above a critical field strength. However, as shown by Uguz et al. (2008), for a certain range of fluid properties the electric field could be stabilizing due to the subtle role of the surface charge.

Experimental studies of the electric-driven interfacial instability have a long history and go as far back as the mid-eighteenth century. Despite that, some of the fundamental aspects of the phenomena are still not reasonably well understood. Here, we do not provide a detailed account of the literature and only refer to a study by Dong et al. (2001) which is particularly relevant to the present work. These authors studied the formation of liquid columns on liquid-liquid interface under a transverse electric field for several different fluid systems. When the applied voltage was low, no column was formed but the interface started oscillating. For sufficiently high voltage, liquid columns were formed that rose from the fluid with higher electric conductivity and penetrated into the liquid with lower conductivity. The columns

were not uniformly distributed and moved and twisted irregularly on the interface, with rotation about the column axis. Furthermore, some of the columns were not vertical. When the applied voltage was further increased the columns were drawn higher and finally connected to the top electrode. The total number of the columns, their average diameter, height, and slenderness ratio were found to increase with an increase in the applied voltage.

The numerical simulations of the problem in the context of leaky dielectric liquids are more recent and limited to only a few studies. Here a notable work is due to Collins et al. (2008) who studied the mechanism of cone formation, jet emission, and breakup during tip-streaming due to a transverse electric field. To expedite the formation of the cones, the authors used a forcefocusing approach where they exposed only a narrow region around the middle of the thin liquid film to an electric potential difference using an electrode that was placed right above the middle of the liquid film. The authors developed a scaling law to predict the size of the drops that were produced from the jet break up. Furthermore, based on the simulation results they concluded that tip-streaming would not develop if the fluids were perfectly insulating or perfectly conducting. Another relevant undertaking in this regard is due to Sharifi and Esmaeeli (2008) who studied formation of liquid columns at the interface of two-superimposed liquids in an essentially unbounded domain. The results of this study showed growth of a liquid column, which originated from a symmetric sinusoidal perturbation and extended from the more conducting fluid toward the less conducting one. For sufficiently large surface tension, the column resembled a cone with a base that spanned the lower electrode. However, when the surface tension was reduced sufficiently, the column transferred to a slender cylinder with droplets ejecting from its tip.

Since in many microfluidic applications the film is confide by a wall, it is of interest to determine the effect of film thickness on the dynamics. To this end, we perform several representative simulations where the thickness of the lower layer is changed from one simulation to the other. We also examine the evolution of the flow structure toward the steady state. The simulation results are interpreted using the pertinent theoretical relations.

## 2  Linear Stability Analyses

In what follows we provide a brief account of the interface instability using EHS and EHD models. This analysis is essential for understanding the numerical results as well as the selection of the individual physical parameters.

We begin our analysis by considering the interface instability using EHS model where the fluids are treated as perfectly insulating and inviscid. Figure (1) depicts a
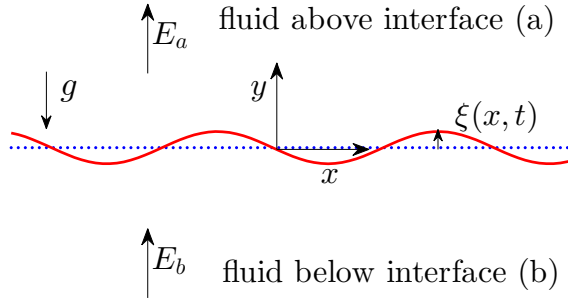
Figure 1: Schematic of a perturbed interface in an infinite domain.

fluid system comprising two horizontal fluid layers of infinite extension, subjected to a transverse electric field where the lighter fluid is overlaid on top of the heavier one. Here subscripts *a* and *b* are used to identify the quantities associated with the upper and lower fluids, respectively. The interface is initially flat and in the absence of the electric field, the fluid system is stable in a Rayleigh-Taylor sense; i.e., perturbations in the form of waves with small amplitude introduced at the interface will die off. To explore the circumstances under which the fluid system becomes unstable, the flat interface is perturbed by a wave that is characterized by $\xi = Re[\hat{\xi} exp(\omega t - ikx)]$, where $\hat{\xi}$ is the complex amplitude $k$ is a real number denoting the wavenumber, $t$ is time, and $\omega = \omega_r + i\omega_i$ is an inverse time constant, which is in general a complex number. $i$ is the imaginary unit, and $Re$ stands for the real part of a complex expression. Using the method of normal modes, where a perturbation series solution is used for the dependent parameters in the linearized equations (continuity, momentum, and electric field equations), results in the following equation for $\omega$ (the so-called dispersion relation) as a function of the input parameters:

$$\omega^2 = \frac{k^2}{\rho_a + \rho_b}\left[f_e - \frac{\Delta\rho g}{k} - \gamma k\right], \tag{1}$$

where

$$f_e \equiv f_{e,PDM} = \frac{(\varepsilon_a - \varepsilon_b)^2 E_a E_b}{\varepsilon_a + \varepsilon_b}. \tag{2}$$

Here $E_a$ and $E_b$ represent, respectively, the normal components of the electric field strength [Vol/m] in the upper and the lower layers in the base state; i.e., before introduction of the perturbation. Note that $E_a$ and $E_b$ are uniform in each layer. In the above equations $\varepsilon$ denotes the electric permittivity, $\gamma$ is the surface tension, $g$ is

the gravity, $\Delta\rho = \rho_b - \rho_a > 0$, and PDM stands for perfect dielectric model. $f_e$ is the electric force per unit area, which in EHS model is solely due to dielectrophoretic effects resulting from the mismatch of the electric permittivities of the two fluids. As is evident from Eq. (1), for a typical wave of wavenumber $k$, as long as the electric field strength is below a certain threshold (or the so called critical field), $\omega^2 < 0$ and the interface will remain stable. However, if the electric field strength goes beyond the critical field, $\omega^2 > 0$ and the interface becomes unstable. The critical field associated with each wavenumber can be found by setting $\omega^2 = 0$ in Eq. (1), yielding:

$$f_{e_{cr}}(E(k),\varepsilon) = \frac{\Delta\rho g}{k} + \gamma k. \tag{3}$$

Considering the continuity of electric displacement field at the interface for perfect dielectric fluids ($\varepsilon_a E_a = \varepsilon_b E_b$), Eq. (3) yields the critical electric field strength in the upper and lower layers, respectively:

$$
\begin{aligned}
E_{cr_a}^2(k) &= \left(\frac{\varepsilon_b}{\varepsilon_a}\right)\frac{\varepsilon_a + \varepsilon_b}{(\varepsilon_a - \varepsilon_b)^2}\left[\frac{g\Delta\rho}{k} + \gamma k\right], \\
E_{cr_b}^2(k) &= \left(\frac{\varepsilon_a}{\varepsilon_b}\right)\frac{\varepsilon_a + \varepsilon_b}{(\varepsilon_a - \varepsilon_b)^2}\left[\frac{g\Delta\rho}{k} + \gamma k\right].
\end{aligned}
\tag{4}
$$

Here, $k$ inside the parentheses is used for $f_{e_{cr}}(E(k),\varepsilon)$, $E_{cr_b}^2(k)$, and $E_{cr_a}^2(k)$ to emphasize that these critical quantities are associated with a particular wave $k$.

Figure (2) shows the variation of $E_{cr_a}(k)$ versus $k$ for three different $\tilde{\varepsilon} = \varepsilon_b/\varepsilon_a$. Here, the properties are $\rho_a = 1$, $\rho_b = 4.7807$, $g = 2$, $\varepsilon_a = 1 \times 10^{-5}$, $\varepsilon_b = 2 \times 10^{-4}$, and $\gamma = 0.5$. As is evident, the required electric field to destabilize the small wavenumbers is very large and increases nearly linearly for large wavenumbers, while it passes through a minimum in between.

This is because for small wavenumbers, the surface tension is weak and the electric force is balanced by the buoyancy ($E_{cr}(k) \sim 1/\sqrt{k}$), while for large wavenumbers, the buoyancy is weak and the electric force is balanced by the surface tension ($E_{cr}(k) \sim \sqrt{k}$). The figure suggests that the variations of $E_{cr}(k)$ with $\tilde{\varepsilon}$ is not monotonic and a larger electric field is needed when the permittivities of the two fluids are of the same order. This can be justified by considering Eq. (4), where it is seen that $E_{cr}(k)$ is more influenced by the difference in, rather than the ratio of, the permittivities.

To determine the minimum critical electric field strength $E_{cr,min}$, we set $df_{e_{cr}}/dk = 0$ in Eq. (3), leading to:

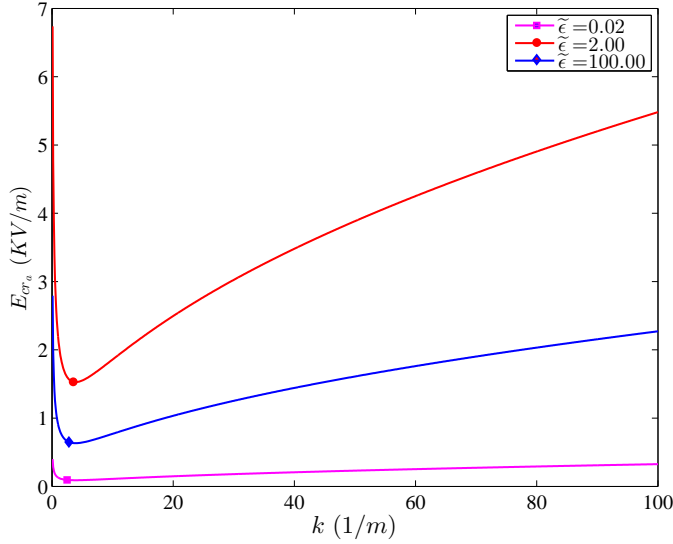$$f_e(E_{cr,min},\varepsilon) = 2\sqrt{g\Delta\rho\gamma}, \tag{5}$$

Figure 2: Variation of critical electric field with wavenumber for three different permittivity ratios.

where the wavenumber associated with the minimum critical electric strength is:

$$k = \sqrt{g\Delta\rho/\gamma} \equiv k_{cr}. \tag{6}$$

Considering the continuity of the electric displacement field at the interface ($\varepsilon_a E_a = \varepsilon_b E_b$) in Eq. (5), the minimum critical electric strengths in the upper and the lower layers are found to be:

$$
\begin{aligned}
E_{cr,min_a}^2 &= 2\sqrt{g\Delta\rho\gamma}\left(\frac{\varepsilon_b}{\varepsilon_a}\right)\frac{\varepsilon_a + \varepsilon_b}{(\varepsilon_a - \varepsilon_b)^2}, \\
E_{cr,min_b}^2 &= 2\sqrt{g\Delta\rho\gamma}\left(\frac{\varepsilon_a}{\varepsilon_b}\right)\frac{\varepsilon_a + \varepsilon_b}{(\varepsilon_a - \varepsilon_b)^2}.
\end{aligned} \tag{7}
$$

A few observations regarding the preceding results are in order. First, the wavelength associated with the minimum critical electric field strength (Eq. (6)) is the same as the Rayleigh inviscid wavelength. This is intuitively understandable because at the threshold of the instability the weight of the fluid (encapsulated in the protrusion) $g\Delta\rho/k^3$ is balanced by the restoring force of surface tension $\gamma/k$. Second, in practical applications one is generally interested in the critical voltage $\Delta\varphi_{cr}$ across the two layers rather than the critical electric field strengths in each layers. If we assume that the upper and the lower electrodes are at distances

$h_a \equiv a$ and $h_b \equiv b$ from the initially flat interface, then $\Delta \varphi_{cr} \sim E_{cr,min_a} a + E_{cr,min_b} b$. Third, the term $\sqrt{g \Delta \rho \gamma}$, which appears in Eqs. (5)-(7) can be interpreted as $\sqrt{F_B} \times \sqrt{F_S} \sim \sqrt{\Delta \rho g l_s} \times \sqrt{\gamma / l_s}$, where $F_B$ and $F_S$ are the buoyant force and the surface tension (per unit area) and $l_s$ is a suitably defined length scale. Since $f_e \sim \varepsilon E^2 [\text{N}/\text{m}^2]$ represents the electric force per unit area, this observation in conjunction with Eq. (5) signifies the fact that the electric force must overcome the restoring forces of buoyancy and surface tension to sustain the instability. It also points to the fact that $\varepsilon E^2 / \sqrt{g \Delta \rho \gamma}$ is an intrinsic nondimensional number for the problem at hand. Fourth, when the electric field strength is below the critical field strength, $\omega$ is imaginary ($\omega^2 < 0$), which results in a traveling wave. In this case, the electric field leads to undulation of the interface. Accordingly, when the electric field is slowly raised, it is expected to see undulations of the interface followed by formation of the columns (see, for example, Dong et al. 2001).

A question that naturally arises is that for a given fluid system and an electric field that is larger than the critical field (i.e., $f_e > 2 \sqrt{g \Delta \rho \gamma} \equiv f_e(E_{cr,min}, \varepsilon)$), what is the range of the possible waves that will be excited? To answer this question, the starting point is again the dispersion relation given in Eq. (1). Here, we set $\omega^2 = 0$, but this time we solve for the wavenumber $k$. This yields $-k^2 + f_e(k/\gamma) - k_{cr}^2 = 0$, solution of which results in:

$$k_L = \frac{f_e - \sqrt{f_e^2 - 4g \Delta \rho \gamma}}{2\gamma}; \quad k_U = \frac{f_e + \sqrt{f_e^2 - 4g \Delta \rho \gamma}}{2\gamma}, \quad (8)$$

where $k_L$ and $k_U$ are the lower and upper wavenumbers of the waves $k_L \leq k \leq k_U$ that will be excited. Of all the waves that become unstable, the wavenumber of the one with the fastest growth rate (the most unstable wavenumber) is particularly of interest. This is found be by setting $d\omega^2/dk=0$ in Eq. (1), yielding:

$$k_{max,e} = \frac{f_e + \sqrt{f_e^2 - 3g \Delta \rho \gamma}}{3\gamma}. \quad (9)$$

It should be noted that $k_L < k_{cr} < k_{max,e} < k_U$ and also $f_e > 2\sqrt{g \Delta \rho \gamma} \equiv f_e(E_{cr,min}, \varepsilon)$ in order for $k_{max,e}$ to be real.

In summary, the net result of the EHS model is that the transverse electric field is always "destabilizing" once its strength is above the minimum critical electric field strength.In particular, since $k_{cr} < k_{max,e}$, then $k_{max,0} = k_{cr}/\sqrt{3} < k_{max,e}$. Therefore, electric field can excite waves whose wavelengths are smaller than the most unstable two-dimensional Rayleigh inviscid wavelength $\lambda_{max,0}$. The relative significance of $f_e$ compared to the restoring force of buoyancy and surface tension $\sqrt{g \Delta \rho \gamma}$ is a determining factor in setting the relation between $\lambda_{max,e}$ and $\lambda_{max,0}$. The strik-

ingly simple structure of $f_e$ is due to the simplifications inherent in EHS model in conjunction with the inviscid flow assumption.

While the EHS model can correctly predict the dynamics for some fluid systems, it will lead to results that are incompatible with experimental studies for some other fluid systems. This is because the formation of the free charge and the associated force is ignored in this model. Smith and Melcher (1967) were the first to study interfacial instability of leaky dielectric fluids. These authors used a linear stability analysis and were able to find a general dispersion relation, which should be solved numerically. Here, we describe a special case that is relevant to our study and is also amenable to a closed form solution. This case was also analyzed by Smith and Melcher (1967). In the spirit of EHD, the conductivity $\sigma$ and the viscosity $\mu$ of the fluids should be included in the analysis. As a result of exposition to the electric field, a volume charge is formed inside the two fluids, which migrates gradually to the interface. The volume charge can be excluded from the analysis if we assume that the electrical relaxation time in both fluids ($\varepsilon_a/\sigma_a$ and $\varepsilon_b/\sigma_b$) are much shorter than the time scale of the motion of the interface $1/|\omega|$. If we further assume that the dynamical time scale $1/|\omega|$ in turn is much larger than the time scale of viscous diffusion ($1/k^2\nu_a$, $1/k^2\nu_b$), the general dispersion relation can be simplified to:

$$D(\omega,k) \equiv (\rho_a+\rho_b)\omega^2 + \left[2k^2(\mu_a+\mu_b)\right]\omega + \left[g\Delta\rho k + \gamma k^3 - k^2 f_{e,LDM}\right] = 0, \quad (10)$$

where

$$f_{e,LDM} = \varepsilon_a E_a^2\left[\frac{\left(\tilde{\varepsilon}/\tilde{\sigma}^2-1\right)\left(1-\tilde{\sigma}\right)}{\tilde{\sigma}+1} + \frac{2\left(1-\tilde{\varepsilon}/\tilde{\sigma}\right)^2\left(1+\tilde{\varepsilon}/\tilde{\sigma}\right)}{2\left(\tilde{\sigma}+1\right)^2 M + \left(1-\tilde{\varepsilon}/\tilde{\sigma}\right)^2\left(1+\tilde{\sigma}\right)}\right], \quad (11)$$

Here, $M = \sigma_a\mu_a(1+\tilde{\mu})/(\varepsilon_a E_a^2)$ and LDM stands for Leaky Dielectric Model. From Eq. (10)-(11) it is evident that the relative magnitudes of the permittivity and conductivity ratios, $\tilde{\varepsilon}$ and $\tilde{\sigma}$, plays a key role in setting the magnitude of the electric force. Compared to the dispersion relation for perfect dielectric fluids (i.e., Eq. (1)-(2)), here the coefficient of $\omega$ is not zero because the effect of viscous forces are accounted for. Furthermore, the structure of $f_e$ is more involved. As before, the electric field that leads to the incipience of instability for a given wavenumber $k$ can be found by setting $\omega = 0$ in Eq. (10), yielding $k^2 - f_{e,LDM}(k/\gamma) + k_{cr}^2 = 0$, where $k_{cr} = \sqrt{g\Delta\rho/\gamma}$. This equation can be solved to determine $f_{e,LDM}$ as a function of the wavenumber:

$$f_{e,LDM} = \gamma\left(k + \frac{k_{cr}^2}{k}\right), \quad (12)$$

which is the same as Eq. (3), except for the fact that $f_e \equiv f_{e,PDM}$ has been replaced by $f_{e,LDM}$.

To find the minimum critical electric field strength and the associated wavenumber, we set $df_{e,LDM}/dk = 0$ in Eq. (12), yielding the critical electric pressure:

$$f_{e,LDM}(E_{cr,min}, \varepsilon, \sigma, \mu) = 2\sqrt{\Delta \rho g \gamma}, \tag{13}$$

and the associated critical wavenumber

$$k = \sqrt{g \Delta \rho / \gamma} \equiv k_{cr,LDM}. \tag{14}$$

Considering the continuity of the electric current at the interface $(\sigma_a E_a = \sigma_b E_b)$ a relation similar to Eq. (7) can be derived for the minimum critical electric field strength in leaky dielectric fluids:

$$\frac{\varepsilon_a E_{cr,min_a}^2}{\sqrt{\Delta \rho g \gamma}} = \left( (1 - \alpha \Sigma) + \left[ (1 + \alpha \Sigma)^2 + 4 \delta \Sigma \right]^{1/2} \right) \beta^{-1}, \tag{15}$$

where

$$\begin{aligned}
\alpha &= \left( \frac{\tilde{\varepsilon}}{\tilde{\sigma}^2} - 1 \right) (1 - \tilde{\sigma}) \left( 1 - \frac{\tilde{\varepsilon}}{\tilde{\sigma}} \right)^{-2}, \\
\delta &= 2 \left( 1 + \frac{\tilde{\varepsilon}}{\tilde{\sigma}} \right) \left( 1 - \frac{\tilde{\varepsilon}}{\tilde{\sigma}} \right)^{-2}, \\
\beta &= 1 + \frac{\tilde{\varepsilon}}{\tilde{\sigma}^2}, \\
\Sigma &= \left( \frac{\sigma_a}{\varepsilon_a} \right) \frac{\mu_a + \mu_b}{\sqrt{\Delta \rho g \gamma}}.
\end{aligned} \tag{16}$$

It should be noted that the wavenumber associated with the minimum critical electric strength is the same as the Rayleigh inviscid critical wavenumber and that $E_{cr,min_b} = \sigma_a E_{cr,min_a} / \sigma_b$.

As pointed out earlier, when the applied electric field strength is larger than the critical one, a collection of waves will become unstable. To find the wavenumbers associated with these waves we use a similar procedure as before by solving $k^2 - f_{e,LDM}(k/\gamma) + k_{cr}^2 = 0$ for $k$. This results in an upper bound $k_{U,LDM}$ and a lower bound $k_{L,LDM}$ that have formally the same structure as the corresponding equations for the perfect dielectric fluids, except that $f_e$ is now replaced by $f_{e,LDM}$.

To find the wavenumber of the wave with the maximum growth, $k_{max,LDM}$, we take the derivative of the terms in Eq. (10) with respect to $k$ and set $d\omega/dt = 0$ in the resulting equation. We then need to solve the resulting equation and Eq. (10) numerically. Figure (3) shows the variation of the growth rate with the wavenumber

for a leaky dielectric fluid and a perfect dielectric fluid. Here, the properties are $\rho_a = 1$, $\rho_b = 4.7807$, $g = 2$, $\sigma_a = 2 \times 10^{-4}$, $\sigma_b = 2 \times 10^{-3}$, $\varepsilon_a = 1 \times 10^{-5}$, $\varepsilon_b = 2 \times 10^{-4}$, and $\gamma = 0.5$. Since the goal was to compare the effect of electric properties, we did not account for the fluid viscosities in plotting these curves.
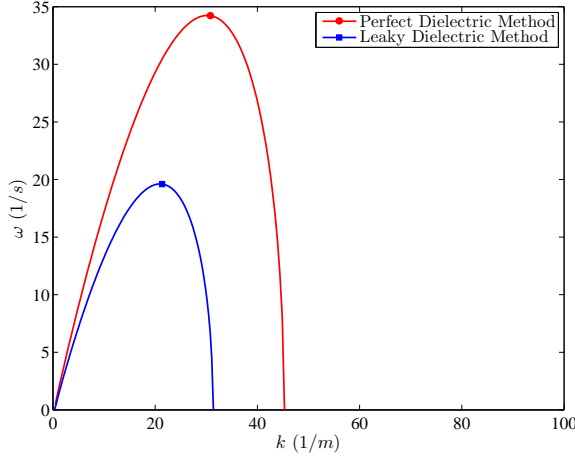


Figure 3: Variation of growth rate with wave number using leaky dielectric model and prefect dielectric model.

For the range of the parameters that are used here the unstable region based on the leaky dielectric model is substantially smaller than that based on the perfect dielectric model. Furthermore, the growth rate based on the former is almost half of that based on the latter

While a transverse electric field always plays a destabilizing role according to EHS model, this is not the case if EHD model is used. This was shown by Uguz et al. (2008) who derived the normal stress balance at the interface at the first order of the perturbation for a linearized system of equations and showed that the sign of the net normal electric stress is the same as the sign of the capillary force for fluid systems if $(\tilde{\varepsilon}/\tilde{\sigma}^2 - 1)(1 - \tilde{\sigma}) < 0$, reflecting the fact that the electric force is stabilizing the perturbations. Inspection of Eq. (15)-(16) lends some support to their analysis. Here, the second term in the bracket in Eq. (15) is always positive, but the first term $1 - \alpha\Sigma$ can be negative or positive, depending on the sign of $\alpha \sim (\tilde{\varepsilon}/\tilde{\sigma}^2 - 1)(1 - \tilde{\sigma}) < 0$. For $\alpha < 0$, $1 - \alpha\Sigma > 0$ and $E_{cr}$ will be larger compared with the case when $\alpha > 0$, suggesting that a larger electric field is needed to destabilize the interface in the former fluid system.

It is worth mentioning that the EHD-based results will converge to EHS-based ones

in the limit of $\tilde{\sigma} = \tilde{\varepsilon}$. This is because this limit is tantamount to elimination of the free surface charge and the associated tangential shear stress.

## 3   Problem Setup

The problem setup is shown in Figure (4), depicting two superimposed fluid layers that reside in a two-dimensional computational domain of size $W \times H$. The domain is periodic in the horizontal direction and wall-bounded in the vertical direction. The light fluid is overlaid on top of the heavy one and a uniform electric field is established by setting the top and the bottom walls at fixed electric potentials of $\varphi_{top}$ and $\varphi_{bot}$, respectively. Here, $\varphi_{top} > \varphi_{bot}$, therefore, the electric potential gradient is upward and the electric field strength is downward. Experimental results show that the polarity of the electric field generally does not play a major role in the results. This is also the case for the EHD (as well as the EHS) model since the electric force is invariant with respect to the direction of the gradient of the electric potential.
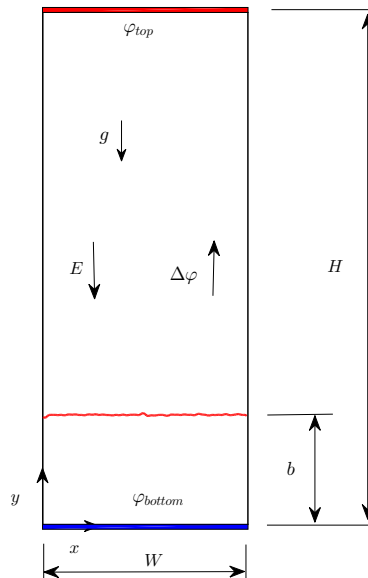


Figure 4: The problem setup depicting two superimposed liquid layers exposed to a transverse electric field.

## 4  Mathematical Formulations and Numerical Method

### 4.1  Mathematical Formulations

The governing equations for this problem are the momentum conservation, the mass conservation, and the electric field equations. These equations should be solved for each fluid and are coupled together through the jump conditions at the interface. Rather than writing the governing equations separately, we use the so-called "one-fluid" formulation where a single set of equations is written for all the fluids involved. The phase boundary is treated as an embedded interface by adding the appropriate source terms to the conservation laws. These source terms are delta functions localized at the interface and are selected in such a way to satisfy the correct matching conditions at the interface. The resulting one-fluid Navier-Stokes equation is:

$$\rho\left(\frac{\partial \mathbf{u}}{\partial t} + \nabla\cdot(\mathbf{u}\mathbf{u})\right) = -\nabla p + \rho\mathbf{g} + \nabla\cdot\left[\mu\left(\nabla\mathbf{u}+(\nabla\mathbf{u})^{T}\right)\right]$$
$$+ \gamma\int \mathbf{n}_f \kappa_f \delta(x-x_f)dS_f + \mathbf{F}_{elec}. \tag{17}$$

Here we have used the conventional notation; $\mathbf{u}$ is the velocity, $p$ is the pressure, $\mathbf{g}$ is the gravity, $\rho$ is the density, and $\mu$ is the viscosity. The force due to the surface tension is represented by the integral over the surface of the phase boundary; $\gamma$ is the surface tension, $\kappa$ is the curvature, $\mathbf{n}$ is a normal unit vector at the interface, $\delta$ delta is a two-dimensional delta function, and $dS$ is the differential arclength of the interface. The variables with subscript $f$ are evaluated at the interface; $\mathbf{x}$ is the point at which the equation is evaluated and $\mathbf{x}_f$ is the position of the interface.

To incorporate the effect of electric field, we need to compute the electric force per unit volume $\mathbf{F}_{elec}$. For leaky dielectric fluids the electric forces are confined only to the interface of the fluids. As such, it is more appropriate to consider these forces as arising from a stress tensor. This is done by considering the electric force as the divergence of an electric stress tensor $\mathbf{F}_{elec} = \nabla\cdot\tau_M$, where $\tau_M$ is the so-called Maxwell stress tensor (Landau and Lifshitz, 1985):

$$\tau_M = \varepsilon\mathbf{E}\mathbf{E} - \frac{1}{2}\varepsilon\mathbf{I}\mathbf{E}\cdot\mathbf{E}. \tag{18}$$

For a general dynamic system, the basic laws of electricity and magnetism are coupled together and are represented by Maxwell's equations (Stratton, 2007). However, in the absence of an external magnetic field, and for very small dynamic electrical currents, it is possible to ignore the degree of magnetic induction and to decouple the electric and magnetic field. As shown by Saville (1997), this is true for

a fairly wide class of problems. If it is further assumed that the time scale of charge relaxation from the bulk to the surface by conduction is smaller than any process time of interest, the electric field equations can be also decoupled from the fluid flow equations. Under the above conditions, the equation for conservation of free charge leads to the following one-fluid equation for the electric potential:

$$\nabla \cdot \sigma \nabla \varphi = 0, \tag{19}$$

where the electric field is obtained from the electric potential by $\mathbf{E} = -\nabla\varphi$.

The momentum equation is supplemented by the mass conservation equation, which for incompressible flows is simply:

$$\nabla \cdot \mathbf{u} = 0. \tag{20}$$

Since the material properties are different for the different fluids, it is necessary to track the evolution of these fields by solving the equations of state, $Ds/Dt = 0$, where $s$ represents density, viscosity, conductivity, and permittivity. Here, however, we assume that the material properties are constant within each phase, so once the interface position is known, these variables can be set.

It is important to recognize that the single-fluid formulation satisfies the conventional governing equations and naturally incorporates the correct jump conditions across the interface (see, for example, Esmaeeli and Tryggvason, 2004). Thus, Eq. (17) leads to the conventional momentum equations in each fluid away from the interface, where the delta function is zero. Integration of this equation over a very thin volume that encompasses and moves with the interface results in the following jump conditions across the interface in the normal

$$-[\![p]\!] + [\![\tau_{nn}^h]\!] + \gamma\kappa + [\![\tau_{nn}^e]\!] = 0, \tag{21}$$

and the tangential directions

$$[\![\tau_{nt}^e]\!] - [\![\tau_{nt}^h]\!] = 0. \tag{22}$$

Here

$$[\![Q]\!] = Q_a - Q_b \tag{23}$$

represents the jump in a typical physical parameter $Q$ across the interface where we have assumed that the unit vector normal at the interface points toward the upper fluid. $\tau^h$ and $\tau^e$ are the hydrodynamic and Maxwell stress tensors, respectively. The subscript $t$ and $n$, respectively, stand for the directions normal and tangent to the interface. Similarly, the jump conditions associated with Eq. (19) are $[\![E_t]\!] = 0$ and $[\![\sigma E_n]\!] = 0$, and are implicitly satisfied in our methodology.

### 4.2 Numerical Method

We work with two sets of grids: a stationary grid and a moving/unstructured one. The stationary grid is used to discretize the governing equations. The moving grid marks the position of the phase boundary and is used to keep the stratification of material properties sharp and to calculate the surface tension. This grid is also used to advect the fluid/fluid phase boundary by interpolating the velocities of the marker points from the regular grid.

The computations start with meshing the interface and setting the materials properties of both fluids. We then solve Eq. (19) for the electric potential and find the electric field using $\mathbf{E} = -\nabla\varphi$. Equation (18) is then used to calculate the Maxwell electric stress and the electric force $\mathbf{F}_{elec} = \nabla \cdot \tau_M$. This term is then added to the right hand side of Eq. (17). To solve the Navier-Stokes equation, we use a standard projection algorithm where we split the momentum equation into two parts. The first part is a prediction step where the effect of pressure is ignored:

$$\frac{\mathbf{u}^* - \mathbf{u}^n}{\Delta t} = \frac{1}{\rho^n} \mathbf{A}(\mathbf{u}^n),$$  (24)

and the second part is a correction step where the pressure gradient is added:

$$\frac{\mathbf{u}^{n+1} - \mathbf{u}^*}{\Delta t} = -\frac{1}{\rho^n} \nabla_h p.$$  (25)

Here, $\mathbf{A}$ is a term that bulks the discrete advection, diffusion, surface tension, and electric force terms in the Navier-Stokes equations, and $\mathbf{u}^*$ is a provisional velocity field in the absence of pressure. The subscript $h$ denotes the finite difference numerical approximation. The pressure is determined in such a way that the velocity at the next time step is divergence free:

$$\nabla_h \cdot \mathbf{u}^{n+1} = 0.$$  (26)

To find the pressure, we take the divergence of Eq. (25) and use Eq. (26), resulting:

$$\nabla_h \cdot \frac{1}{\rho^n} \nabla_h p = \frac{\nabla_h \cdot \mathbf{u}^*}{\Delta t}.$$  (27)

This equation is solved using a multigrid iteration method and the velocity field is corrected by including the pressure effects:

$$\mathbf{u}^{n+1} = \mathbf{u}^* - \frac{1}{\rho^n} \Delta t \nabla_h p.$$  (28)

The method as described above is first order in time and second order accurate in space. However, in the numerical implementation, we use a predictor/corrector algorithm which makes the method second order accurate in time. See, Esmaeeli and Tryggvason (2004) for more details regarding the time integration.

## 5 Selections of the Individual Parameters and the Governing Nondimensional Numbers

As we pointed out earlier, for leaky dielectric fluids the electric field will be destabilizing, provided the fluid properties are such that $(\tilde{\varepsilon}/\tilde{\sigma}^2 - 1)(1 - \tilde{\sigma}) < 0$ and the applied electric field strength $E_0 \sim (\varphi_t - \varphi_b)/H$ is larger than $E_{cr,min}$. Under this circumstance, perturbations with wavenumbers in the range $k_L \leq k \leq k_U$ will grow, with $k_{max,e}$ having the largest growth rate. To ensure excitation of at least a few waves the width of the computational domain $W$ and the applied electric field strength $E_0$ should be chosen appropriately. Here, we have chosen $W = \lambda_d$, where $\lambda_d \equiv \lambda_{max,0} = \sqrt{3}\lambda_{cr}$ is the most unstable two-dimensional Rayleigh inviscid wavelength. Since $\lambda_{max,e} < \lambda_{max,0}$, we expect to see the growth of a few waves. To choose the applied electric potential difference $\Delta\varphi = \varphi_t - \varphi_b$, we performed the following procedure. First, we estimated the critical electric field strengths $(E_{cr_a,LDM}, E_{cr_b,LDM})$ that would destabilize a perturbation of wavelength $\lambda_{max,0}$ using Eq. (12). Then we increased the estimated value by about 10-30%. Subsequently, we used the solution for the electric potential of two horizontal superimposed fluid layers of thicknesses $a$ (upper) and $b$ (lower), separated by a flat interface, and solved for $\Delta\varphi$ using $E_{cr_a,LDM}$ or $E_{cr_b,LDM}$ as an input parameter. This yielded:

$$\Delta\varphi = \frac{CE_{cr_a,LDM}(\sigma_b a + \sigma_a b)}{\sigma_b}, \tag{29}$$

where $C$ is the coefficient that accounts for the percentage of increase of the estimated value. To allow for the sufficient growth of the perturbations, the height of the domain was chosen as $H = 2.5W$.

The individual parameters that govern the problem are $\rho, \mu, \sigma, \varepsilon, \gamma, \Delta\rho g, E_0, b$, and $H$. We use the capillary length scale $l_s = \sqrt{\gamma/g\Delta\rho}$ as our primary length scale and the properties of the lower fluid to construct our nondimensional numbers. To proceed, we also need to choose a velocity scale. Two intrinsic velocity scales exist; a primary scale and a secondary one. The primary velocity scale is constructed based on the fact that the fluid flow is established as a result of a balance between the electric shear stress $\tau_{xy}^e$ and the viscous shear stress $\tau_{xy}^h$ at the interface. The electric shear stress $\tau_{xy}^e$ scales as $q_s E_s$, where $q_s$ is a free electric surface charge scale and $E_s$ is an electric field strength scale. Considering $q_s \sim \varepsilon_s E_s$ and $E_s \sim \Delta\varphi/H$, results in $\tau_{xy}^e \sim \varepsilon_s(\Delta\varphi)^2/H^2$. Then the balance of the viscous shear stress $\tau_{xy}^h \sim \mu_s u_s/l_s$ with $\tau_{xy}^e$ leads to the velocity scale $u_s = (l_s\varepsilon/\mu)(\Delta\varphi/H)^2$, which upon substitution for the properties of the lower fluid becomes $u_s = (l_s\varepsilon_b/\mu_b)(\Delta\varphi/H)^2$. The secondary velocity scale is $u_s^b \sim \sqrt{l_s g}$, which is a velocity scale based on the flow that is driven by the buoyancy.

Nondimensionalization of the individual parameters leads to the flow Reynolds number $Re_f = \rho_b u_s l_s / \mu_b$, the electric Weber number $We = \rho_b u_s^2 l_s / \gamma$, nondimensional lengths, $\tilde{b} = b/l_s$, $\tilde{H} = H/l_s$, and the ratio of material properties $\tilde{\rho} = \rho_b/\rho_a$, $\tilde{\mu} = \mu_b/\mu_a$, $\tilde{\sigma} = \sigma_b/\sigma_a$, and $\tilde{\varepsilon} = \varepsilon_b/\varepsilon_a$. Furthermore, the electric Reynolds number $Re_{el} = \tau_C/\tau_P$ is also an independent nondimensional number. This parameter is the ratio of the charge relaxation time (maximum of $\tau_{C_a} = \varepsilon_a/\sigma_a$ and $\tau_{C_b} = \varepsilon_b/\sigma_b$) to the process time of interest $\tau_P$, and is not the subject of parametric study when leaky dielectric model is used. However, it should be sufficiently small to guarantee that the leaky dielectric model is applicable. The process time of interest in our simulations is the time that it takes a liquid column to form, which is reasonably larger than $\tau_C$. When we present our results, unless stated otherwise, we use $l_s = \sqrt{\gamma/g\Delta\rho}$, $u_s = (l_s\varepsilon_b/\mu_b)(\Delta\varphi/H)^2$, and $t_s = l_s/u_s$ as our length, velocity and time scales.

## 6 Results

### 6.1 Effect of Film Thickness on the Formation of Liquid Columns

To investigate the effect of film thickness, we performed several simulations in the computational domain depicted in Fig. (4). Here, the only difference between these simulations was the thickness of the lower liquid layer $b$, which was changed from one simulation to the other. To trigger instability, the flat interface was perturbed by a series of random waves described by:

$$y = b + \frac{a}{N} \sum_{n=1}^{N} R(n) \left[ \cos\left(2\pi nx/W\right) + \sin\left(4\pi nx/W\right) \right], \tag{30}$$

where $b$ is the average initial thickness of the film, $N = 15$ is the number of waves, $a = 0.02\lambda_{max,0}$ is the initial amplitude of the waves, and $0 \leq R(n) \leq 1$ is a number determined by a random number generator. For all the simulations $\lambda_{max,0} \equiv \lambda_d = 2.8$, and the domain size was $W \times H = 2.8 \times 7$. Based on the grid refinement studies, a $128 \times 320$ grid was used to resolve the flow. The nondimensional numbers for these simulations are $Re_f = 1.58 \times 10^4$, $We = 9.9896 \times 10^4$, $\tilde{H} = 27.237$, $\tilde{\rho} = 4.7807$, $\tilde{\mu} = 2.591$, $\tilde{\sigma} = 10$, and $\tilde{\varepsilon} = 20$. In what follows, we describe the results of three representative simulations.

We start our analysis by considering the behavior of the interface in a moderately thick lower layer. Figure (5) shows contours of the electric potential along with the interface for this simulation at a few selected times. Here, $\tilde{b} = 5.836$, or in terms of the width of the domain, $b/W=0.536$. The variations of the electric potential at the interface is a determining factor in setting the strength and distribution of the free

surface charge and the net electric stresses. The ratio of the electric conductivities plays a major role in setting the magnitude of the electric potential at the interface.
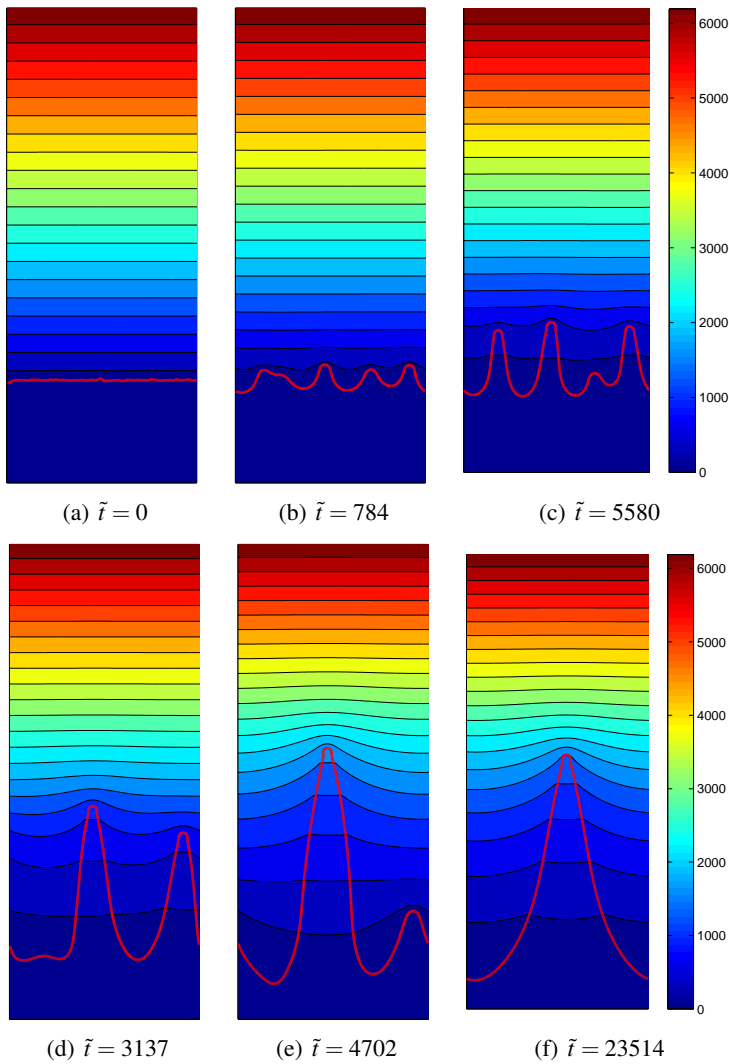


Figure 5: Contours of electric potential along with the interface for a moderately thick lower liquid layer. Here, $\tilde{b} = 5.836$ and $b/W = 0.536$.

Since the conductivity of the lower layer is much higher than that of the upper one, the electric potential is relatively uniform in this layer but changes linearly from

the interface to the top electrode in the upper layer. This is evident from the concentration of the contourlines in the frames. Accordingly, the electric field strength is weak in the lower layer and strong in the upper one. The interface is initially flat, but its surface is rough because of the perturbations that were introduced. The surface tension, however, stabilizes the short waves, providing incentive for the growth of the longer waves. This results in formation of four waves (frame b). Since the lower liquid is heavier, it penetrates into the upper one in the form of spikes, while the top liquid penetrates into the lower one in the form of bubbles. The competition between the four columns leads to the growth of three of the columns while one of them hardly grows (frame c). As time progresses, binary competition between the columns (i.e., counting from the left to the right, columns 1 and 2, and columns 3, 4) leads to suppression of two of them (frame d). The competition between the remaining two columns (frame e) leads to the formation of a large column (frame f). From this point onward, the interface settles to a steady-state, where the electric force is balanced by the buoyancy and the surface tension.

The instability is driven by the nonuniformity of the electric forces at the interface. Here, a slight protrusion of the initially flat interface into the upper or the lower liquid leads to a locally higher or lower, respectively, electric field strength at the surface of the protrusion. This is because the electric potential difference is essentially between the interface and the top electrode due to the high conductivity of the lower fluid. Accordingly, the electric force is stronger at the peaks compared to valleys, resulting in the growth of the instability. The relevant wavelengths for this simulation are listed in Table (1). The entries in this table were found by plugging the electric field strengths based on the one-dimensional solution $|E_a| = \Delta\phi\sigma_b/(\sigma_b a + \sigma_a b)$, $|E_b| = \sigma_a|E_a|/\sigma_b$, into Eq. (2), (8), and (9), and the corresponding equations for the LDM. Here $\lambda_{max,e}/\lambda_{max,0} = 3.664$, so we expect to see excitation of at least three waves. The wavelengths of the incipient waves are in line with the prediction from the linear theory, as shown in Fig. (6)b and reported in the caption of this figure.

Table 1: The relevant wavelengths for the simulation with a moderately thick lower liquid layer.

| $\tilde{b} = 5.836$ | $\lambda_L$ | $\lambda_U$ | $\lambda_{max,e}$ |
|---|---|---|---|
| Leaky Dielectric | 0.353 | 7.384 | 0.764 |
| Perfect Dielectric | 0.277 | 9.432 | 0.415 |

Figure (6) shows the velocity field for this simulation. The fluid is initially quiescent, but as a result of the imbalance of the electric shear stresses fluid flow is

initiated at the interface and is amplified by the growth of the protrusions. Once the protrusions become sufficiently large to turn into distinct waves (frame b), two counter-rotating vortices appear per wave. The fluid flow around the waves is upward at the peaks and downward at the valleys. As the waves grow further to form columns, two new vortices are formed around the top of the columns, while the original vortices grow larger and are displaced downward (frame c). The senses of the newly formed vortices are opposite to those of the original neighboring ones. A similar vortical structure is seen in frames (d) and (e). At steady state (frame f), the flow field consists of two large vortices at the sides of the columns in the outside, which are joined by their counterparts inside the column. Here, the velocity vectors do not cross the interface, reflecting the fact that the interface is stationary.

The strength and distribution of the free electric charge is a determining factor in the interface instability since it profoundly affects the strengths of the net normal and tangential electric stresses. Figure (7) shows contours of the free electric charge and vectors of the electric force $\mathbf{F}_{elec}$ at the interface. Initially the charge distribution is uniform (when the interface is flat) but it becomes nonuniform as the protrusions grow. For a given electric potential gradient, the sign of the surface charge depends on the relative magnitude of $\tilde{\sigma}$ and $\tilde{\varepsilon}$. For $\tilde{\sigma} < \tilde{\varepsilon}$, the sign of the charge correlates positively with the electric field potential difference $\Delta\varphi$. The opposite is true for $\tilde{\sigma} > \tilde{\varepsilon}$. Here, $\tilde{\sigma} < \tilde{\varepsilon}$ and $\Delta\varphi > 0$, thus the sign of the charge is positive as can be seen from the figure. The magnitude of the charge depends on the local electric field strength. As can be seen from the figure, the magnitude is the lowest at the base and the highest at the tip, in line with the distribution of the electric field strength at the interface. The electric force scales with the square of the electric field strength. Accordingly, it is strongly affected by the non-uniformities of the electric field strength at the interface. Thus, the electric force is the lowest at the base and the highest at the tip. The outward sense of the vector forces signifies the fact that the electric force provides the necessary pull to sustain the weight of the column and the resorting force of the surface tension.

We now turn our attention to a simulation where the lower layer is thin. We keep all the nondimensional parameters the same and decrease the nondimensional film thickness to $\tilde{b} = 1.167$, corresponding to a thickness to width ratio of $b/W = 0.107$. Here the "nominal" applied electric strength $E_0 \sim \Delta\varphi/H$ is the same as that for the first simulation, however, since the lower layer is much more conducting than the upper one, the "effective" electric field strength is much lower. Accordingly, the range of the unstable wavelengths $\lambda_L < \lambda < \lambda_U$ and the most unstable wavelength $\lambda_{max,e}$ are, respectively, smaller and larger than the corresponding values for the first simulation. Table (2) shows the relevant wavelengths for this simulation. Here $\lambda_{max,e}/\lambda_{max,0} = 2.62$, so we expect to see excitation of at least two

(a) $\tilde{t} = 0$  (b) $\tilde{t} = 784$  (c) $\tilde{t} = 5580$

(d) $\tilde{t} = 3137$  (e) $\tilde{t} = 4702$  (f) $\tilde{t} = 23514$
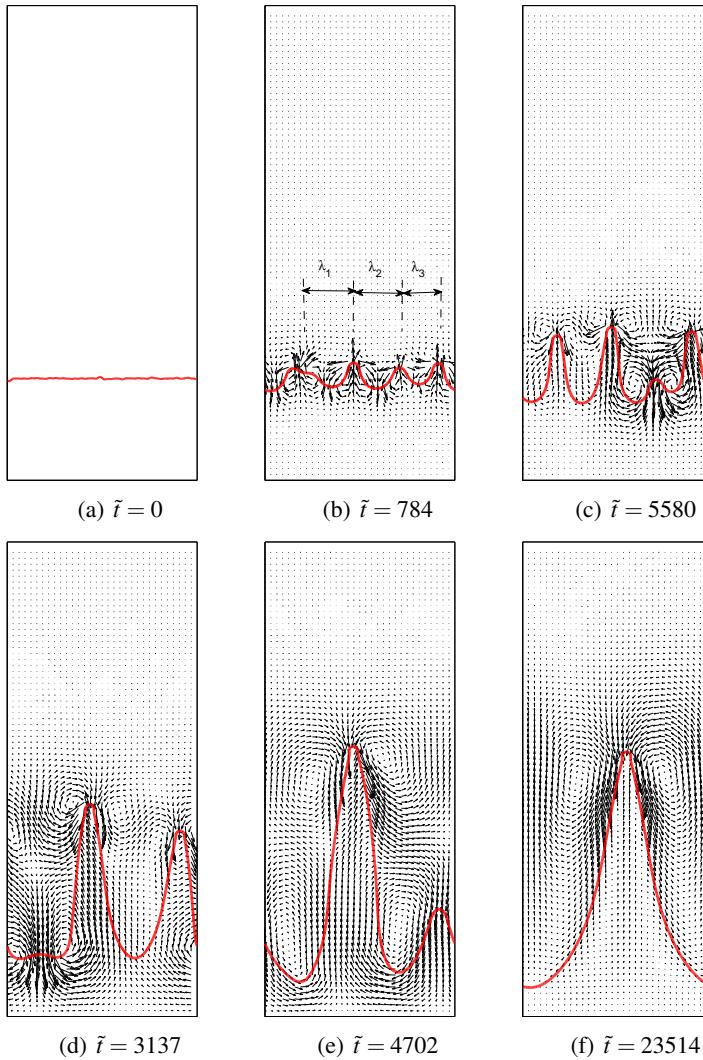
Figure 6: Velocity vectors and the interface for a moderately thick lower liquid layer. To aid visualization, the velocity vectors are drawn at every third grid points. Here, $\tilde{b} = 5.836$, $b/W = 0.536$, and the wavelengths of the incipient waves are $\lambda_1 = 0.823\lambda_{max,e}$, $\lambda_2 = 0.886\lambda_{max,e}$, and $\lambda_3 = 0.738\lambda_{max,e}$.

waves. The wavelengths of the incipient waves are in line with the prediction from the linear theory, as shown in Fig. (8)b and reported in the caption of this figure.
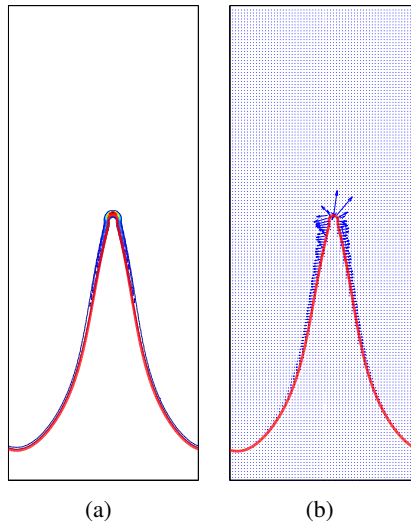
(a)                    (b)

Figure 7: Contours of free electric charge and vectors of electric forces corresponding to the last frame of Fig. (5).

Table 2: The relevant wavelengths for the simulation with a thin lower liquid layer.

| $\tilde{b} = 1.167$ | $\lambda_L$ | $\lambda_U$ | $\lambda_{max,e}$ |
|---|---|---|---|
| Leaky Dielectric | 0.543 | 4.805 | 1.067 |
| Perfect Dielectric | 0.416 | 6.276 | 0.624 |

Figure (8) shows selected frames from the evolution of the velocity field and the interface during this simulation. As before, the surface tension stabilizes the small scale disturbances, leading to the growth of longer waves (frame b).

Compared to the first simulation, here the lower wall strongly influences the competitions between the waves as it prevents the downward growth of the protrusions. Here, three waves emerge (frame c) and the competition between them leads to two relatively long columns that are separated by a shorter one (frame d). As time progresses the longer columns grow and in the process suppress the growth of the shorter one (frame e), leading to two columns that are connected together at their bases through a thin liquid film. The columns grow further until the lubrication forces in the liquid film prevent further thinning of the film (frame f).

In the third simulation, we consider a very thick lower layer by positioning the interface closer to the top wall, resulting in $\tilde{b} = 15.564$ and $b/W = 1.429$. Table
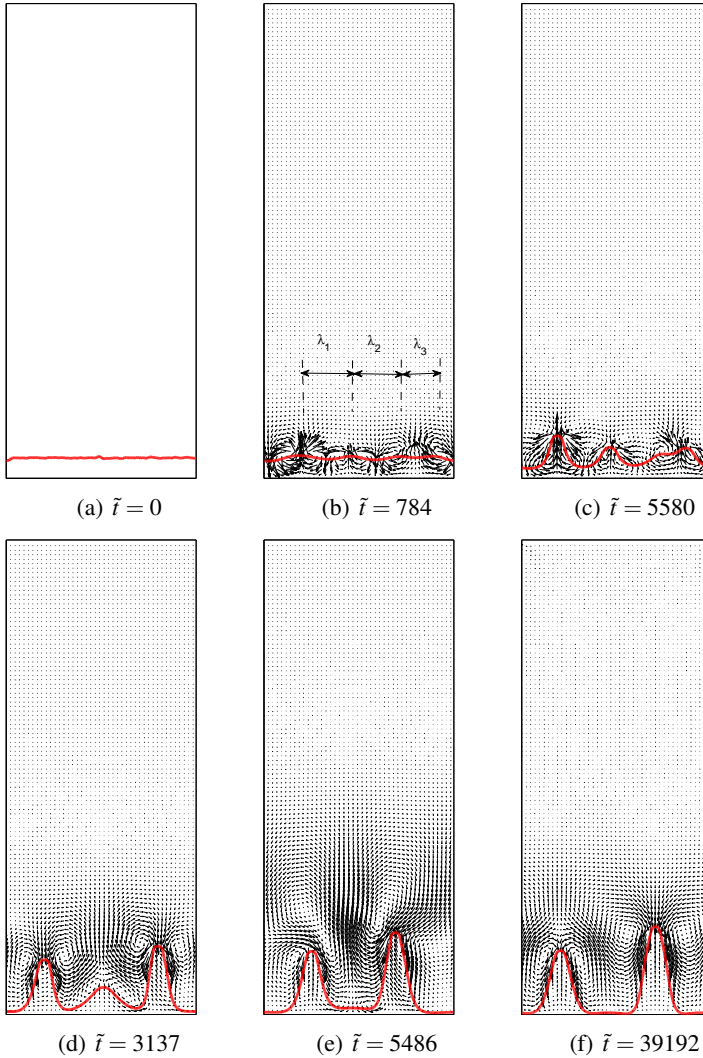
Figure 8: Velocity vectors and the interface for the simulation with a thin lower liquid layer. To aid visualization, the velocity vectors are drawn at every third grid. Here, $\tilde{b} = 1.167$, $b/W = 0.107$, and the wavelengths of the incipient waves are $\lambda_1 = 0.743\lambda_{max,e}$, $\lambda_2 = 0.688\lambda_{max,e}$, and $\lambda_3 = 0.449\lambda_{max,e}$.

(3) shows the wavelengths relevant to this simulation. Here $\lambda_{max,e}/\lambda_{max,0} = 9.271$, so we expect to see excitation of at least nine waves.

Table 3: The relevant wavelengths for the simulation with a very thick lower liquid layer.

| $\tilde{b} = 15.564$ | $\lambda_L$ | $\lambda_U$ | $\lambda_{max,e}$ |
|---|---|---|---|
| Leaky Dielectric | 0.112 | 23.313 | 0.302 |
| Perfect Dielectric | 0.089 | 29.38 | 0.133 |

Figure (9) shows the velocity field and the interface for this simulation at selected times. Here, the system did not settle to a steady state since a few of the columns



(a) $\tilde{t} = 0$         (b) $\tilde{t} = 390.7$         (c) $\tilde{t} = 784.19$
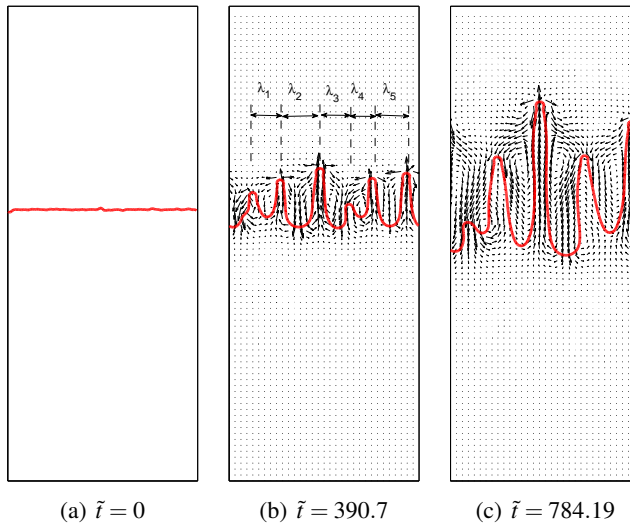
Figure 9: Velocity vectors and the interface for a very thick lower liquid layer. To aid visualization, the velocity vectors are drawn at every third grid point. Here, $\tilde{b} = 15.564$, $b/W = 1.429$, and the wavelengths of the incipient waves are $\lambda_1 = 1.366\lambda_{max,e}$, $\lambda_2 = 3.323\lambda_{max,e}$, $\lambda_3 = 1.497\lambda_{max,e}$, $\lambda_4 = 1.076\lambda_{max,e}$, and $\lambda_5 = 1.697\lambda_{max,e}$

grew so rapidly that they anchored the upper wall. Compared to the previous simulations, where the shapes of the columns were conical, here the columns are cylindrical. Furthermore, one of the columns is not quite upright and is tilted toward the left (frame c), suggesting a stronger interactions between the columns. Both of these effects are due to the stronger interfacial normal electric forces. Frame (b) shows the wavelengths of the emerging waves. Here the larger magnitude of the

wavelengths with respect to $\lambda_{max,e}$ is due to the fact that this frame represents a more advanced stage in the stability growth compared to the previous two simulations.

### 6.2 Effect of Film Thickness and Applied Voltage on the Kinetic Energy

As we observed in the preceeding simulations, the fluid flow does not cease at steady state when the interface becomes stationary. As such, the structure of the flow and its strength are of interest in microfluidic applications that involve enhancement of mixing by electric field. Among the parameters that affect the flow strength, the film thickness and the applied electirc voltage are particularly important because they affect the dynamics more directly. Here we have run two sets of simulations to explore the effect of these parameters. In the first set, we used the same nondimensional parameters as those used in Section 6.1 and performed a few simulations at several film thicknesses other than those used in Section 6.1. We then calculated the steady state kinetic energy $KE = (1/2) \int \rho (u^2 + v^2) dA$ of the system for these simulations. In the second set, we used the same fluid system as before and a film thickness corresponding to the second simulation ($\tilde{b} = 1.167$) and performed a few simulations at several applied electric voltage $E_0 = \Delta\varphi / H$. Figure (10) shows the variations of nondimensional kinetic energy with nondimensional film thickness. Here the kinetic energy is made nondimensional using $KE_s = \rho_b u_s^2 l_s^2$. Two different behaviors can be distinguished from this figure. For thin and moderately thick films, corresponding to $\tilde{b} \leq \sim 6$, the kinetic energy increases slowly with an increase in the film thickness. However, it increases dramatically once the film thickness passes this threshold. Figure (11) shows the variations of the kinetic energy with the applied electric field strength. This figure was not nondimensionalized since a change in the applied voltage affects two of the nondimensional parameters simultaneously. The results suggest a scaling of the form $KE \sim E_0^{4.7}$, where the exponent is somewhat larger than the scaling that we would expect using the EHD-induced velocity; i.e., $u_s \sim E_0^2 \rightarrow KE \sim E_0^4$. This is presumably because the system did not settle to a steady state at higher electric field, where the interface becomes highly unstable and the simulations are stopped when a liquid column touches the top electrode. The insets show the interface at the same nondimensional intermediate time for the corresponding runs. Note that the second marked point on the curve corresponds to frame (c) of figure 8. As is seen, increasing the applied voltage tends to make the columns more slender; a fact that was also observed in experiments of Dong et al. (2001).
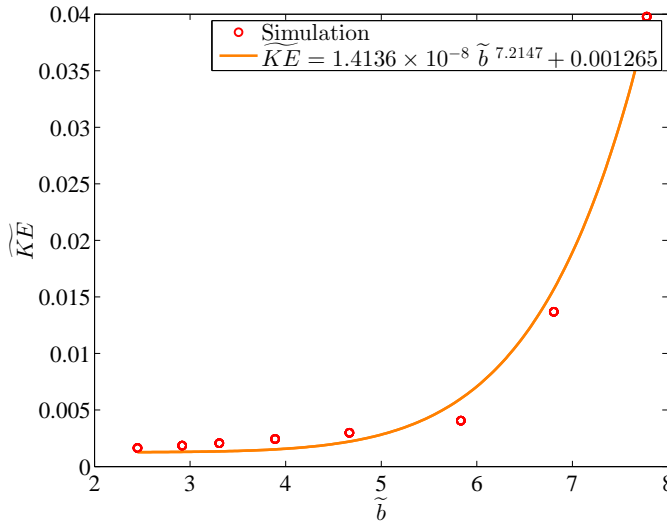
Figure 10: Steady-state kinetic energy of fluids versus the nondimensional initial position of interface $\tilde{b}$. With the exception of the film thickness, all the nondimensional numbers are the same as those used for the three representative simulations.

## 7 Discussion

The analysis of the column formation and the steady state flow structure can be facilitated by examining the net interfacial normal and shear electric stresses in conjunction with the one-dimensional solution of the electric field equation for a flat interface. These stresses are the drivers behind the fluid motion and interface deformation. Using a tangent-normal coordinate at the interface, it can be shown (Esmaeeli and Reddy 2011) that the net normal and tangential electric stresses, respectively, are:

$$
\begin{aligned}
&[\![\tau_{nn}^e]\!] = \frac{\varepsilon_a}{2} \left[ \left(1 - \tilde{\varepsilon}/\tilde{\sigma}^2\right) E_{n_a}^2 + (\tilde{\varepsilon} - 1) E_t^2 \right], \\
&[\![\tau_{nt}^e]\!] = \varepsilon_a E_{n_a} E_t \left(1 - \tilde{\varepsilon}/\tilde{\sigma}\right) = q_s E_t,
\end{aligned}
\tag{31}
$$

where $q_s = \varepsilon_a E_{n_a} (\tilde{\sigma} - \tilde{\varepsilon})$ is the free surface charge. The double bracket denotes the jump according to Eq. (23). The sense of net normal electric stresses is determined by the relative strength of $(1 - \tilde{\varepsilon}/\tilde{\sigma}^2)$ and $(\tilde{\varepsilon} - 1)$. Both terms are positive in our simulation, thus $[\![\tau_{nn}^e]\!] > 0$, which means the direction of the net normal electric force is from the lower fluid toward the upper one. This observation in conjunction with the fact that for $\tilde{\sigma} > 1$ the electric force is stronger at the peaks compared to the valleys, results in the penetration of protrusions in the upper fluid, as is
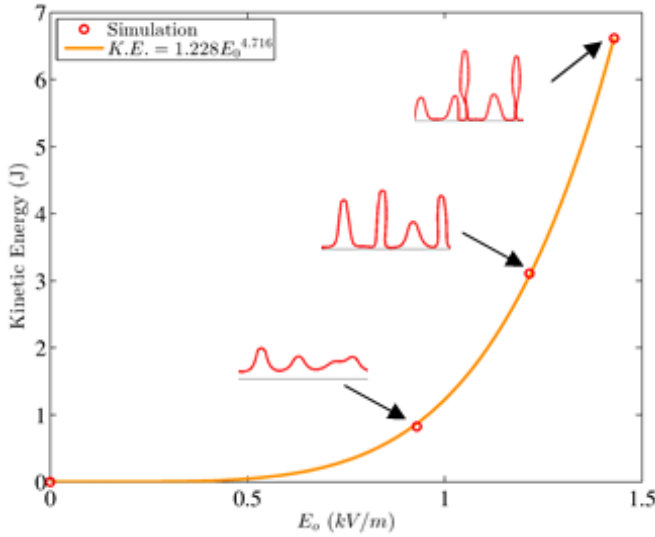
Figure 11: Variations of the kinetic energy of fluids with the applied voltage. Here, $\tilde{b} = 1.167$ and the fluid properties are the same as those used for the first three representative simulations.

evident form the results of the simulations. The formation of the conical columns is initially due to the particular density stratification, which results in penetration of the heavy fluid in the light one in the form of spike and penetration of the light fluid in the heavy one in the form of bubbles. However, at the later stages of growth, the nonuniformity of the electric force distribution at the interface is the main factor in sustaining the conical shapes.

The structure of the fluid flow is determined by the relative magnitude of the shear- and deformation-induced flows. However, at steady state when the interface is stationary, the sense of fluid circulation can be determined solely from the sense of the net electric shear stresses. For instance, for frame (f) of Fig. (6) $[\![\tau_{nt}]\!] < 0$, since $E_{n_a} < 0$ and $E_t < 0$ (based on the direction of $\mathbf{E} = E_t\hat{\mathbf{t}} + E_n\hat{\mathbf{n}}$, which is downward) and the fact that $(1 - \tilde{\varepsilon}/\tilde{\sigma}) < 0$ for our fluid system. This results in a fluid flow along the interface from the tip to the base. Accordingly, when the flow turns around at the interface, a clockwise (counterclockwise) vortex is formed at the left (right) side of the interface outside of the column. These vortices are joined by the counterpart vortices inside the column.

## 8   Conclusion

Direct Numerical Simulations (DNSs) were performed to explore the effect of film thickness on the electric-field driven instability of leaky-dielectric fluids. It was shown that the electric field had destabilizing effect, provided the fluid properties were such that $(\tilde{\varepsilon}/\tilde{\sigma}^2 - 1)(1 - \tilde{\sigma}) < 0$ and the applied electric field strength $E_0 \sim (\varphi_t - \varphi_b)/H > E_{cr,min}$. The electric field led to the excitation of a collection of waves with wavenumbers in the range $k_L \leq k \leq k_U$, with $k_{max,e}$ having the largest growth rate. For a moderately thick film, the excited waves competed to form a large conical column that spanned the width of the computational domain. For a thin film, however, the lower wall strongly influenced the competition between the liquid columns, leading to formation of two columns that were connected together by a thin film. Here, the minimum possible film thickness was the key factor in setting the course of the competition and the steady state shape of the interface. When the film was too thick, the columns grew rapidly until they anchored the top electrode; as a result, the interface did not settle to a steady state. While the simulations were performed for only a fluid system, some of the results can carry over to other fluid systems as well. For instance, for moderately thick lower liquid layer, where the protrusions can grow in both the upward and the downward directions and the resulting columns will not grow so rapidly to touch the top electrode, the competition between the columns will lead to the formation of only one column, regardless of the choice of the fluid system.

## Reference

**Arp, P. A.; Foister, R. T.; Mason, S. G.** (1980): Some electrohydrodynamic effects in fluid dispersions. *Adv. Colloid Interface Sci.,* vol. 12, pp. 295-356.

**Chou, S. Y.; Zhuang, L.** (1999): Lithography induced self-assembly of periodic polymer micropillar arrays. *J. Vac. Sci. Technol. B,* vol. 17, 31973202.

**Collins, R. T.; Jones, J. J.; Harris, M. T.; Basaran, O. A.** (2008): Electrohydrodynamic tipstreaming and emission of charged drops from liquid cones. *Nat. Phys.* vol. 4, pp. 149-154.

**Dong, J.; De Almeida, V. F.; Tsouris, C.** (2001): Formation of liquid columns on liquid-liquid interface under applied electric fields. *J. Colloid Interface Sci.*, vol. 242, pp. 327-336.

**Esmaeeli, A.; Reddy, M. N.** (2011): The electrohydrodynamics of superimposed fluids subjected to a nonuniform transverse electric field. *Int. J. Multiphase Flow,* vol. 37, pp. 1331-1347.

**Esmaeeli, A.; Tryggvason, G.** (2004): Computations of film boiling. Part I: nu-

merical method. *Int. J. Heat Mass Transfer,* vol. 47, pp. 5451-5461.

**Macky, W. A.** (1931): Some investigations on the deformation and breaking of water drops in strong electric fields. *Proc. R. Soc. Lond., Ser. A.*, vol. 133, pp. 565-587.

**Melcher, J. R.; Smith, Ch. V.** (1969): Electrohydrodynamic charge relaxation and interfacial perpendicular-field instability. *Phys. Fluids*, vol. 12, pp. 778-790.

**Melcher, J. R.; Taylor, G. I** (1969): Electrohydrodynamics: A review of the role of interfacial shear stresses. *Annu. Rev. Fluid Mech.*, vol. 1, pp. 111-147

**Melcher, J. R.** (1963): *Field Coupled Surface Waves.* MIT Press, Cambridge.

**Melcher, J. R.; Schwarz, W.** (1968): Interfacial relaxation overstability in a tangential electric field. *Phys. Fluids*, vol. 12, pp. 2604-2616.

**O'Konski, C. T.; Harris, F. E.** (1957): Electric free energy and the deformation of droplets in electrically conducting systems. *J. Phys. Chem.,* vol. 61, pp. 1172-1174.

**O'Konski, C. T.; Thacher, H. C.** (1953): The distortion of aerosol droplets by an electric field. *J. Phys. Chem.,* vol. 57, pp. 955-958.

**Saville, D. A.** (1997): Electrohydrodynamics: The Taylor-Melcher leaky dielectric model. *Annu. Rev. Fluid Mech.*, vol. 29, pp. 27-64.

**Schaffer, E.; Thurn-Albrecht, T.; Russell, T. P.; Steiner, U.** (2000): Electrically induced structure formation and pattern transfer. *Nature,* vol. 403, 874877.

**Sharifi, P.; Esmaeeli, A.** (2008): Computational Studies on behavior of an interface separating two fluids under uniform electric field. FDSM2008-55191. Proceedings of ASME fluid engineering division summer conference, August 10-14, 2008, Jacksonville, FL.

**Smith, C. V.; Melcher, J. R.** (1967): Electrohydrodynamically induced spatially periodic cellular Stokes-Flow. *Phys. Fluids*, vol. 10, pp. 2315-2322

**Stone, H. A.; Stroock, A. D.; Ajdari, A.** (2004): Engineering flows in small devices: microfluidics toward a lab-on-chip. *Ann. Rev. Fluid Mech.*, vol. 36, pp. 381-411.

**Stratton, J. A.** (2007): *Electromagnetic Theory.* Wiley-Interscience, New York.

**Taylor, G. I.** (1966): Studies in electrohydrodynamics: I. The circulation produced in a drop by an electric field. *Proc. R. Soc. London, Ser. A*, vol. 291, pp. 159-167.

**Uguz, A. K.; Ozen, O.; Aubry, N.** (2008): Electric field effect on two-fluid interface instability in channel flow for fast electric times. *Phys. Fluids,* vol. 20, 031702.

**Yeoh, H. K.; Xu, Q.; Basaran, O. A.** (2007): Equilibrium shapes and stability of a

liquid film subjected to a nonuniform electric field. *Phys. Fluids,* vol. 19, 114111.

**Zaghdoudi, M. C.; Lallemand, M.** (2002): Electric field effects on pool boiling. *J. Enhanc. Heat Transf.,* vol. 9, pp. 187-208.

**Zeng, J.; Korsmeyer, T.** (2004): Principles of droplet electrohydrodynamics for lab-on-a-chip. *Lab. Chip,* vol. 4, pp. 265-277